PSFC/JA-16-74

Impurity screening behavior of the high-field side scrape-off layer in near-double-null configurations: prospect for mitigating plasma-material interactions on RF actuators and first-wall components

B. LaBombard, A.Q. Kuang, D. Brunner, I. Faust, R. Mumgaard,
M.L. Reinke*, J.L. Terry, N.Howard, J.W. Hughes, M. Chilenski, Y. Lin,
E. Marmar, J.E. Rice, P. Rodriguez-Fernandez, G.Wallace, D.G. Whyte,
S. Wolfe, S. Wukitch

*Oak Ridge National Laboratory, Oak Ridge, TN 37831, USA

December 2016

Plasma Science and Fusion Center
Massachusetts Institute of Technology
Cambridge MA 02139 USA

This work was supported by DoE Contract DE-FC02-99ER54512 on Alcator C-Mod, a DoE Office of Science user facility.

Impurity screening behavior of the high-field side scrape-off layer in near-double-null configurations: prospect for mitigating plasma-material interactions on RF actuators and first-wall components

B. LaBombard†, A.Q. Kuang, D. Brunner, I. Faust, R. Mumgaard, M.L. Reinke[1], J.L. Terry, N. Howard, J.W. Hughes, M. Chilenski, Y. Lin, E. Marmar, J.E. Rice, P. Rodriguez-Fernandez, G. Wallace, D.G. Whyte, S. Wolfe, S. Wukitch

MIT Plasma Science and Fusion Center, Cambridge, MA, USA.
[1]Oak Ridge National Laboratory, Oak Ridge, TN 37831, USA

†labombard@psfc.mit.edu

Abstract

The impurity screening response of the high-field side (HFS) scrape-off layer (SOL) to localized nitrogen injection is investigated on Alcator C-Mod for magnetic equilibria spanning lower-single null, double-null and upper single null configurations under otherwise identical plasma conditions. L-mode, EDA H-mode and I-mode discharges are investigated. HFS impurity screening is found to depend on magnetic flux balance and the direction of B×∇B relative to the most active divertor. Impurity 'plume' emission patterns indicate that both parallel and perpendicular (E×B) flows in the SOL contribute to the 'flushing' of impurities towards the active divertor, thereby affecting the overall impurity screening behavior. Despite the fact that the HFS scrape-off layer is extremely narrow in near-double-null configurations, this SOL is able to screen locally injected nitrogen at least as effectively as the low-field side (LFS) SOL – up to a factor of 10 more effective, depending on specific plasma conditions and whether the magnetic geometry produces parallel flows that work with or against E×B flows. For situations in which the E×B drift of the impurity ions opposes parallel flow toward the primary divertor, HFS impurity screening is found to be least effective. When E×B drifts assist parallel flow toward the primary divertor, HFS impurity screening is found to be very effective. These data support the idea of placing RF actuators and close-fitting wall components on the high-field side of the tokamak. With this configuration, near-double-null magnetic topologies may be used for active control of plasma parameters at the antenna/plasma interface for optimal RF coupling, mitigate the generation of local impurities from plasma-material interactions and, taking advantage of favorable plasma flows and good screening properties of the HFS SOL, further minimize the impact of wall-born impurity sources on the plasma core.

1. Introduction

Robust physics and technology solutions to control plasma-material interactions (PMI) on main-chamber components, including RF actuators, must be demonstrated in order to develop credible designs for steady-state, electricity generating fusion reactors. For the tokamak concept, RF-based current drive and heating technologies are considered the most reactor-relevant technologies in terms of efficiency (wall-plug to plasma), scalability to steady state operation and compatibility with the demands of the nuclear environment (e.g., neutron shielding and tritium breeding). While these systems have demonstrated the ability to replace neutral beams in present physics-oriented experiments, implementing them in a power reactor is thought to be a difficult challenge. Efficient wave coupling necessitates placing RF launchers close to the plasma, which at first sight appears contrary to the idea of minimizing PMI. PMI control is particularly important because component lifetimes will likely dictate the success or failure of a power plant. Unless first wall components, including RF actuators, can survive the PMI onslaught for sufficient time, the power plant will not be economically viable [1].

One promising approach is to locate all RF actuators and close-fitting wall structures on the *high-field side* (HFS) of the tokamak and operate with near-double null magnetic configurations [2-6]. This idea aims to take advantage of some remarkable properties of the HFS SOL: (1) The HFS SOL is a 'quiescent plasma region' with very low levels of turbulence and cross-field transport compared to the low-field side (LFS) [7]; (2) Consequently, in near double-null configurations, density and temperature gradients are very steep and, unlike the LFS, there are no density 'shoulders' that extend out to impact first wall components, including RF actuators; (3) Depending on the degree of upper/lower null balance, the high level of turbulence and cross-field transport that exists on the LFS compared to the HFS produces near-sonic 'transport driven' parallel flows in the HFS SOL [8], which may effectively sweep wall-born impurities into the divertor.

Previous experiments with single null magnetic configurations have shown that nitrogen (N) can be injected at the HFS mid-plane at a rate that is about an order-of-magnitude higher than on the LFS mid-plane, yet produce the same level of core N contamination [9]. This is an exceptional 'impurity screening' ability demonstrated by the HFS SOL. The lack of interchange turbulence on this 'good curvature' side of the torus combined with strong parallel flow to the divertor are believed to be the primary reasons.

From an RF physics and technology point of view, these HFS SOL characteristics (among others listed below) are perhaps the best situation that one could possibly imagine. With RF actuators located on the HFS, operation in near-double-null magnetic configurations could provide unprecedented control of plasma conditions at the antenna/plasma interface via two primary control knobs: upper/lower x-point flux-balance and HFS plasma-antenna gap. These parameters could be tailored – even dynamically, in response to real-time measurements – both to optimize wave coupling and to minimize the level of plasma-material interactions. In addition, if the favorable HFS screening characteristics seen in single-null discharges are found extend to near-double null configurations, then the level of core plasma contamination from residual HFS plasma-wall interactions might be additionally mitigated.

These ideas are particularly compelling because theory and modeling show that RF wave physics considerations are extremely favorable with HFS launch. For the case of lower hybrid current drive (LHCD), the increased magnetic field strength opens up a window in wave accessibility and damping for waves with low parallel wavenumber. As a result, LH waves can penetrate to mid minor radius (critical for current profile control) and at the same time attain a 40% or more increase in current drive efficiency [2, 3, 5, 10, 11] (critical for reducing circulating power and obtaining net electricity production from fusion). A host of other potential benefits has also been identified: energetic particle loads, ELM heat pulses and runaway electron damage on launch structures may be practically eliminated; neutron fluxes to RF launch structures may be minimized, particularly for locations above or below the HFS mid-plane, which is synergistic with optimization of LHCD ray trajectories; a thin, quiescent SOL minimizes undesirable interactions with the SOL (e.g., wave scattering, collisional absorption, parametric decay instabilities); low plasma recycling fluxes lead to low neutral pressures, which are important for maintaining RF voltage standoff. High field side ion cyclotron heating systems (ICRF) would also experience these same advantages while exploiting favorable wave physics in this regime as well [11, 12], such as 100% first pass absorption of fast waves via direct mode conversion.

Motivated by this vision, the Alcator team executed a series of dedicated experiments on Alcator C-Mod during the 2015 and 2016 operational campaigns to examine characteristics of the HFS SOL in detail, focusing on a few key questions: (1) Does the favorable HFS screening behavior extend to balanced double-null configurations where parallel flows become relatively stagnant and the profiles become very narrow? (2) Could it be that operation in a balanced double null configuration is a *disadvantage* with regard to core plasma impurity control? (3) What is the impact of confinement mode (L-mode, H-mode, I-mode) on the impurity screening response?

Based on the experiments described in this paper, we find that the HFS SOL retains good impurity screening characteristics in near-double null configurations despite the formation of extremely narrow scrape-off layers. This result supports the idea of relocating RF actuators to the HFS. However, for topologies away from balanced double-null, the HFS screening response is not always favorable, depending on specific details: the degree of magnetic flux balance, the direction of $\mathbf{B}\times\nabla\mathbf{B}$ relative to the most active divertor and the confinement mode. A subset of these observations was reported at the 2016 Plasma Surface Interaction Conference [13], focusing on ohmic L-mode plasmas and examining profiles in the HFS SOL. Since that time, new impurity screening measurements have been performed for reversed magnetic field (L-mode), EDA H-mode and I-mode cases. This paper compiles and discusses all screening results obtained during C-Mod's operations in 2015 and 2016, thus serving as a final report on this topic.

Section 2 describes the experimental arrangement. Representative HFS and LFS plasma profiles in near-double null configurations are discussed in Section 3. Using these data as input, the location where nitrogen gas ionizes in the HFS and LFS SOLs is examined with the help of a simple 1-D model. The ionization location for sputtered molybdenum and tungsten atoms ($\sim$ 2 eV) is also considered, indicating that the behavior of nitrogen is a reasonable proxy for these wall-born intrinsic impurities. In all cases, the ionization occurs in the SOL, but for the HFS SOL it can occur very close to the last closed flux surface (LCFS). Section 4 describes techniques used to quantify impurity screening, defining an *impurity penetration factor*. The analysis presented for L-modes in [13] are extended to include H-mode discharges with long core

impurity confinement times. For completeness and to provide context for new results, impurity screening observations reported for ohmic L-mode cases [13] are summarized in Section 5, adding new data from reversed magnetic field plasmas. Impurity 'plume' observations are shown, providing insight on the mechanisms that control the overall impurity screening response. New EDA H-mode and I-mode observations are presented in Section 6 for a range of upper/lower null magnetic flux balance. Corresponding impurity 'plume' observations are also discussed. Section 7 summarizes the principal findings of this work.

2. Experimental arrangement

The experimental investigation took advantage of a unique set of diagnostics on Alcator C-Mod [14-16], ideally suited to measure SOL plasmas profiles and to study the core plasma response as nitrogen was injected at the LFS or HFS mid-planes (Fig. 1): fast-scanning probes located on the HFS and LFS mid-planes; capillary tubes delivering calibrated puffs of N_2 gas to the HFS and LFS mid-plane locations; a vacuum ultraviolet (VUV) spectrometer to monitor core plasma nitrogen impurity content.

The scanning probes employed a four-electrode, high heat flux, pyramidal geometry, functioning as Langmuir-Mach probes [17]. High-resolution density, electron temperature and parallel plasma flow profiles up to and slightly inside the last closed flux surface (LCFS) were reported by these systems. Plasma conditions from the HFS scanning probe electrodes were inferred by fitting current-voltage characteristics generated by a 2 kHz triangular voltage sweep. The LFS scanning probe employed a 'mirror Langmuir probe' (MLP) bias system [18, 19], producing measurements of density, electron temperature and parallel plasma flow at 1.1 MHz.

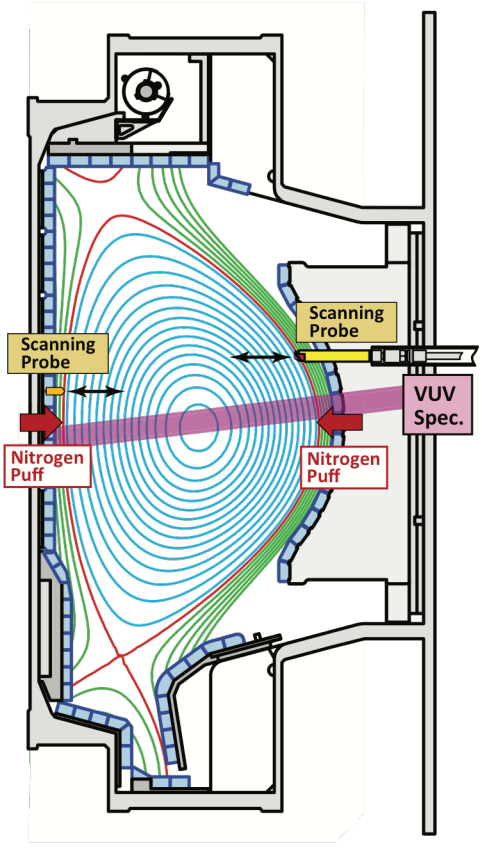

Fig. 1 – Arrangement of HFS and LFS scanning probes, capillary 'gas puff' injectors, and the viewing chord of a VUV spectrometer.

Nitrogen gas was introduced at HFS or LFS mid-plane locations via a capillary injection system [20]. An X-ray Extended Ultraviolet Spectrometer (XEUS) [21] with a central viewing chord (see Fig.1) was used to monitor core plasma N^{5+} and N^{6+} concentrations by recording N VI and N VII line emission over the spectral bands of 2.85-2.98 nm and 2.45-2.52 nm respectively.

In order to account for possible shot-to-shot variation in core plasma impurity confinement time, particularly in H-mode plasmas, the time evolution of Ca impurities injected by a laser blow-off system (CaF_2 target) [22] was monitored on selected discharges. The core plasma impurity confinement time was deduced by fitting an

exponential decay to the brightness of Ca^{18+} and Ca^{19+} recorded by a high resolution x-ray crystal imaging spectrometer [23]. This technique has been used extensively to characterize impurity confinement times for C-Mod plasmas over a wide variety of conditions [24].

Impurity 'plume' emission patterns were monitored from visible light cameras (see Figs. 7 and 8) and a poloidally resolved, UV enhanced photodiode array (Figs. 9, 11, 13) that is sensitive to line emission from N^{4+} ions (discussed further in Section 5.3).

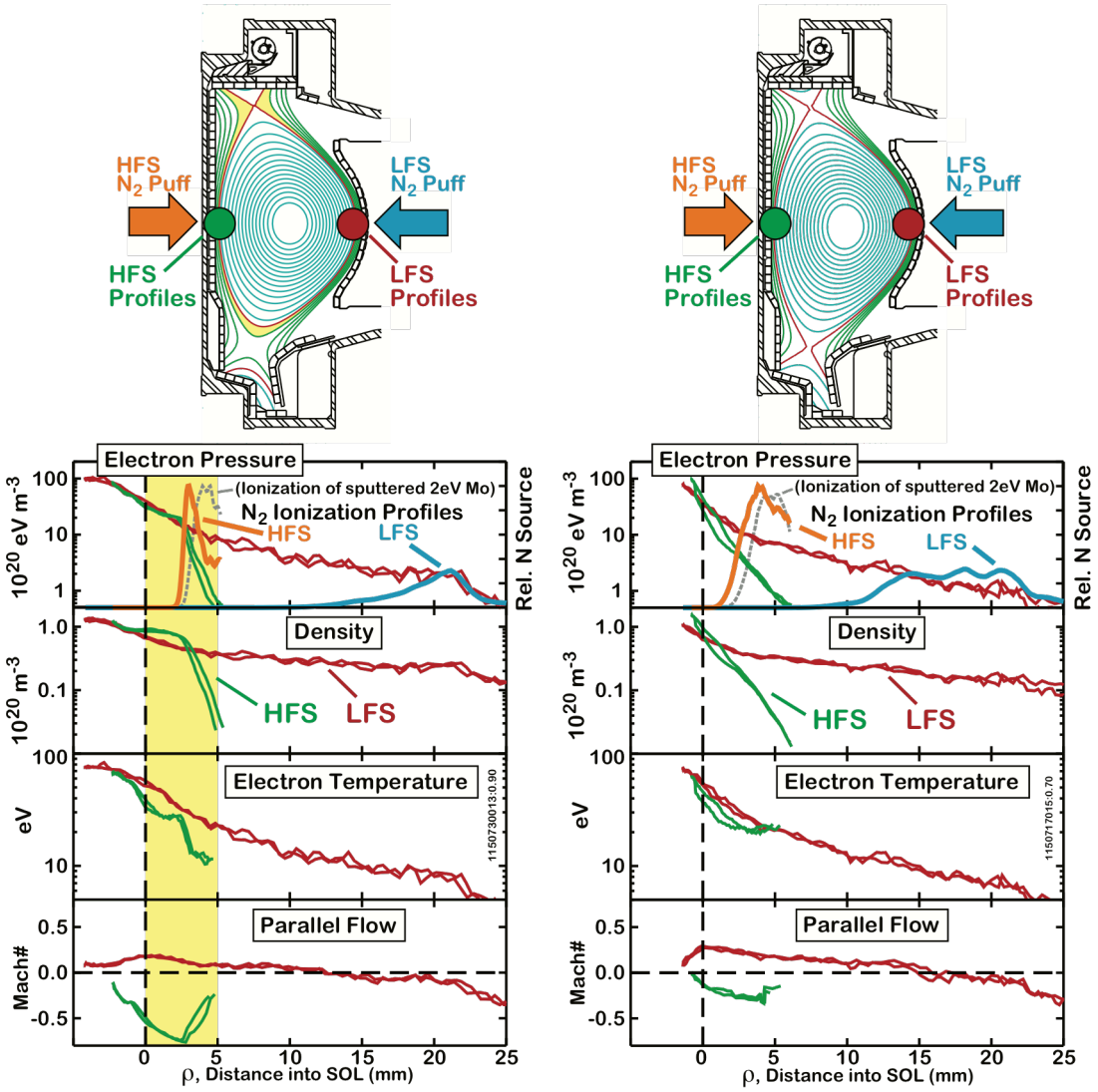

Fig. 2 – Electron pressure, density, electron temperature and parallel flow Mach number profiles for an unbalanced, upper-null dominant equilibrium (left) and a balanced double-null equilibrium (right). The spatial region in which SOL flux surfaces are common to HFS and LFS are highlighted in yellow. Positive Mach number corresponds to flow in the direction of B – towards the divertor on LFS and away from the divertor on HFS. Ionization source profile estimates are shown for HFS (orange) and LFS (cyan) nitrogen injection cases. The ionization source profile for 2 eV molybdenum atoms entering the SOL on the HFS is also estimated (gray dashed lines). Adapted from [13] http://dx.doi.org/10.1016/j.nme.2016.10.006 https://creativecommons.org/licenses/by-nc-nd/4.0/Copyright

3. Plasmas Profiles and Nitrogen Source Location in HFS and LFS SOLs

3.1 Plasma profiles

Plasma profiles and flows in C-Mod's HFS SOL are highly sensitive to magnetic flux balance [7, 8, 25, 26]. At the location where the poloidal magnetic flux surfaces become 'private' to the HFS region, density and temperature profiles in that scrape-off layer develop a very sharp exponential decay. Figure 2 shows HFS/LFS scanning probe measurements from an unbalanced, upper null dominant discharge (left panel), with distance between primary and secondary separatrices of ~5 mm mapped to the outer mid-plane, and a balanced double-null plasma (right panels). Red traces are measurements from the LFS SOL, green traces from the HFS. These two discharges are otherwise identical (0.8 MA, Greenwald fraction 0.2), taken from the ohmic L-mode data set discussed further in Section 5. For the upper-null dominant case, electron pressure profiles approximately match in the zone where flux surfaces are common to HFS and LFS (yellow shaded region). Beyond the flux surface that contains the secondary x-point, electron pressure and density profiles exhibit very sharp decays. Parallel flow Mach numbers on the HFS are very large, approaching 0.8 directed towards the inner strikepoint of the upper divertor.

In contrast, for the balanced double null case, profiles on the HFS and LFS SOLs match only at the LCFS. The sharp decay in the HFS profile begins immediately at the LCFS. Parallel flow Mach numbers on the HFS are reduced in this case, with a maximum value of 0.2 directed toward the upper divertor.

3.2 Nitrogen source location

A scrape-off layer has the potential to 'screen' wall-born impurities from the core only if the impurities ionize in the SOL, i.e., the ionization mean free path is small compared to the SOL width. Using the measured density and electron temperature profiles shown in Fig. 2, a simple estimate was made for the location and shape of the nitrogen ionization source profile, $S(r)$, based on the flux of nitrogen molecules originating at the first-wall (Γ_0). The results of the calculation are shown in Fig. 2 for the HFS (orange) and LFS (cyan traces). As outlined in [13], this estimate considers the spatial attenuation of Γ_0 (at wall temperature) due to N_2 ionization and computes the resultant N source profile based on its spatial derivative,

$$S(r) = \frac{\partial \Gamma_{N_2}}{\partial r} = \Gamma_0 \frac{\partial}{\partial r}\left\{exp\left(-\int_0^r \frac{n_e}{v_0}\langle\sigma v\rangle \partial r\right)\right\}. \quad (1)$$

Because the plasma density at the separatrix in C-Mod is on the order of 10^{20} m^{-3} – the range anticipated for a reactor – the nitrogen ionizes in the SOL at both LFS and HFS locations, despite the sharp profiles. However, the peak location of the N source profiles on the HFS is ~1.5 cm closer to the LCFS. Changing from unbalanced double null to balanced double null additionally shifts the HFS nitrogen source profile toward the LCFS (Fig.2).

It is instructive consider how the behavior of nitrogen impurities in the SOL might act as a proxy for the behavior of intrinsic wall-born impurities, such as molybdenum or tungsten ions, which might arise from sputtering of a HFS RF launcher. Plasma turbulence transport and convection, which is driven by low frequency $E \times B$ motion, is essentially identical for all trace impurity

species. The result of entrainment by SOL parallel plasma flows would also be similar. Therefore an important consideration is the location where molybdenum or tungsten impurities ionize in the SOL compared to nitrogen molecules. For the case of nitrogen gas at room temperature, the average velocity of the molecules directed toward the plasma would be $V_{N2} \sim 470$ m/s. At 10 eV, their ionization rate coefficient is approximately 9.6×10^{-15} m^3/s yielding a mean free path of $\lambda_{N2} \sim 2.4$ mm at a electron density of 2×10^{19} m^{-3}. Sputtered molybdenum ions would have a Thomson distribution [27], with most likely energy in the range of 2 eV ($V_{mo} \sim 2200$ m/s). Because the Mo ionization rate coefficient at 10 eV is a factor of 100 higher, $\sim 1.5 \times 10^{-13}$ m^3/s, the mean free path for ionization is smaller than for nitrogen molecules, $\lambda_{Mo} \sim 0.7$ mm. For tungsten, the sputtered energy and ionization rate is similar to molybdenum but the 2.5 increase in mass produces $V_W \sim 1200$ m/s and $\lambda_W \sim 0.4$ mm. A more careful estimate of the ionization source profile for molybdenum atoms entering into the HFS SOL profiles with an energy of 2 eV is provided in Fig. 2 (dashed gray lines). From these considerations we conclude that the behavior of nitrogen impurities in the SOL is an effective proxy for understanding the behavior of wall-born intrinsic impurities in the SOL.

Based on the ionization source profiles shown in Fig. 2, one might expect HFS nitrogen (and molybdenum or tungsten) screening to become less effective as the magnetic topology is changed from single-null to balanced double null because the 'impurity flushing action' of the SOL parallel flow is reduced and the nitrogen ionization source moves close to the LCFS. However, local fluctuation-induced cross-field particle transport on the HFS SOL is essentially zero, according to direct measurements [7]. Thus the primary question targeted by our investigation arises: Does the very low level of cross-field transport (and by implication, impurity transport) in the 'quiescent' HFS scrape-off layer provide adequate screening of wall-source impurities for balanced double-null discharges? Here an 'adequate' level of impurity screening might be a level that is comparable or better than that observed for the LFS SOL.

From the point of view of optimizing RF coupling and screening of launcher-induced impurities, it appears that slightly unbalanced configurations, such as the *unbalanced, upper-null dominant equilibrium* shown in the left panel of Fig. 2 might be optimum. In this case, very sharp profiles on the HFS are produced while maintaining a strong plasma flow, perhaps sweeping away impurities before they can get into the plasma core. It is remarkable that this situation arises naturally in the SOL; one could not design a better 'puff-and-pump' scheme. However, the underlying physical mechanisms are not so simple. Both parallel and perpendicular flows can contribute to the impurity dispersal in the SOL. Measuring or modeling these flows, including their variation across the SOL, and determining the distribution of wall-born impurities among them would be a formidable task. A more straightforward and reliable way to untangle these physical processes is simply to inject trace impurities into the SOL, vary plasma conditions, including magnetic topology, and record what fraction gets into the plasma core. (As it turns out, based on the research described below, the *unbalanced, upper-null dominant equilibrium* shown in the left panel of Fig. 2 is indeed an optimum arrangement for this magnetic field direction. In this situation, strong parallel flows and $E \times B$ drifts combine to sweep wall-born HFS impurities to the upper divertor.)

4. Computation of impurity penetration factor

Nitrogen is an excellent choice for an impurity tracer in Alcator C-Mod because it behaves as a weak-recycling, non-intrinsic impurity [9] and its spectroscopic emission can be observed by a wide range of standard diagnostic tools. Moreover, the capillary injection system [20] performs calibrated injections at the HFS and LFS mid-plane locations, enabling direct quantitative comparisons of impurity penetration. The analysis presented below follows the one outlined in reference [13], but is extended to account for enhanced core plasma impurity confinement times, as is encountered in H-modes.

Conceptually, the number of nitrogen ions in the confined plasma region (N_N) may be expressed as a flux balance equation applied at the LCFS interface,

$$\frac{\partial N_N}{\partial t} = PF\ \Gamma_N - \frac{N_N}{\tau_p} \quad . \tag{2}$$

In this model, nitrogen gas is injected at the first wall at the rate Γ_N (#/s) and becomes ionized in the local SOL. Through cross-field and parallel transport, the impurity ions disperse in the SOL; some are promptly deposited onto first wall/divertor surfaces while others cross into the confined plasma and contaminate the core. Equation (1) assumes a non-recycling impurity response, i.e., the nitrogen in the core is due to the local impurity injection only, not due to nitrogen recycling at plasma-wall contact locations. The quantity PF Γ_N represents the portion that crosses the LCFS – thus defining a dimensionless *impurity penetration factor*. [Note: the definition of penetration factor used here differs from that defined by McCracken [9], which had units of s^{-1}.] τ_p is a characteristic confinement time for nitrogen impurities in the core plasma. The physical mechanisms that determine PF are, of course, very complex involving: (1) the location in which the impurities are ionized in the SOL, (2) cross-field transport ($E\times B$ drifts, diffusion, convective 'pinches') and (3) the residence time of nitrogen impurities ions in the SOL, which should not be confused with τ_p. See reference [28] for a more complete treatment of this topic. For conceptual simplicity, τ_p is taken as independent of impurity injection location, although in general it need not be. In the latter case, measurements of PF on the HFS versus LFS can be reinterpreted as measurements of the relative *impurity contamination efficiencies* (discussed further below).

The time evolution of nitrogen impurity content in the core plasma can be obtained by integrating Eq. (1), starting from the initial condition of zero impurity content in the core,

$$N_N(t) = PF\ M(\mathrm{t})\ ;\ M(\mathrm{t}) = e^{-t/\tau_p} \int_o^t \Gamma_N\ e^{s/\tau_p} \partial s \quad . \tag{3}$$

For a slowly varying gas injection rate and for times longer than τ_p, the system will achieve a quasi-steady state in which the number of nitrogen ions in the confined plasma is proportional to the injection rate $M(t) = \Gamma_N \tau_p$; $N_N = PF\, \Gamma_N \tau_p$. Figure 3 shows the time behavior of core plasma nitrogen brightness signals (red traces) in response to a nitrogen gas puff in an ohmic L-mode plasma. Background signal levels measured just before the gas injection are subtracted. Since the impurity confinement time, τ_p, is short in L-mode (typically ~20 ms [24]), the brightness signals are expected to be proportional to the gas injection rate, which is slowly varying over this timescale. Also shown in figure 3 are blue traces corresponding to the N_2 gas injection rate, multiplied by appropriate scale factors so as to make these traces overlay with the

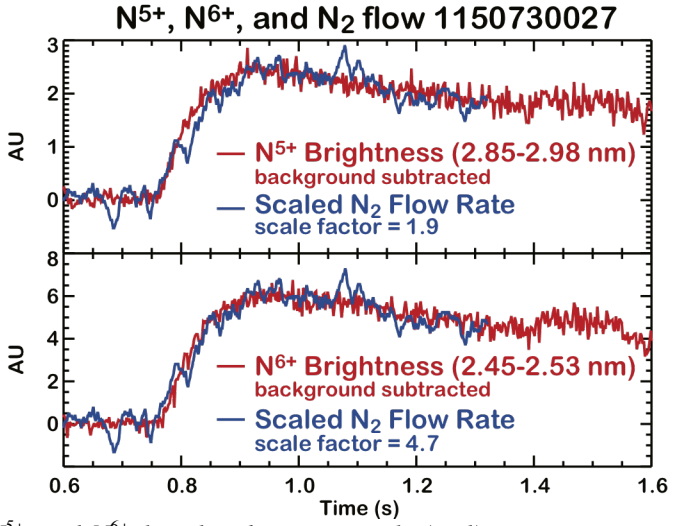

Fig. 3 – N^{5+} and N^{6+} line brightness signals (red) in response to a nitrogen puff from the HFS midplane location in to an L-mode plasma. The signal responses are proportional to N_2 injection flow rate (blue), which is expected for this case of short (L-mode) core impurity confinement time compared to the time evolution of the gas puff. The proportionality constants derived in this way are used as a relative measure of the N impurity penetration factor.

brightness signals. One can see that the red and blue traces do indeed have the same shape. The scale factors so deduced are taken as a relative measure of the impurity penetration factor for the local SOL,

$$Scale\ Factor \propto \frac{N_N}{\Gamma_N} = PF\ \tau_p. \qquad (4)$$

By injecting nitrogen gas from HFS and LFS mid-planes in otherwise identical plasmas, the *ratio of impurity penetration factors*, HFS compared to LFS, can be inferred – it is the *ratio of the scale factors* needed to align gas puff and nitrogen line emission brightnesses. More generally, accounting for the possibility that τ_p depends on impurity injection location, the ratio of scale factors is a measure of the relative contamination efficiencies, $CF = PF\ \tau_p$,

$$\frac{Scale\ Factor|_{HFS}}{Scale\ Factor|_{LFS}} \propto \frac{(PF\ \tau_p)_{HFS}}{(PF\ \tau_p)_{LFS}} = \frac{CF_{HFS}}{CF_{LFS}} \qquad . \qquad (5)$$

For H-modes, this scale factor analysis must include possible corrections arising from non-negligible values of τ_p. In this case $M(t)$, with an appropriate choice of τ_p, may be used as a model function to compare with nitrogen brightness signals. Figure 4 shows the result of performing this analysis for an EDA H-mode plasma with nitrogen injected from the HFS mid-plane location. Laser blow-off measurements performed in identical discharges indicated τ_p values of ~70 ms. Specifically, this measurement was performed using CaF_2 injection, fitting the resultant decay of Ca^{18+} emission recorded by an x-ray crystal spectrometer. Using the value τ_p~ 70 ms, a good alignment is found between nitrogen brightness data (red) and model function data (blue) with appropriate scale factors. Examining data from similar plasmas in the EDA H-mode

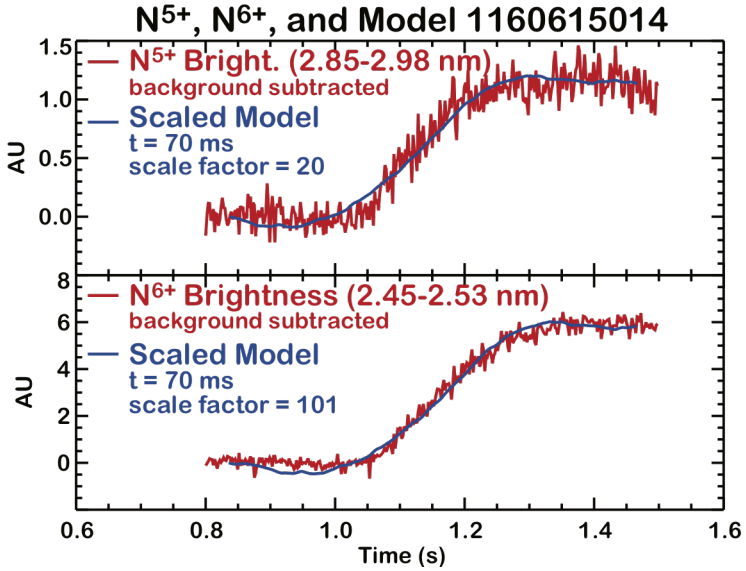

Fig. 4 – N^{5+} and N^{6+} line brightness signals (red) in response to a nitrogen puff from the HFS midplane location in to an EDA H-mode plasma. The signal responses are proportional to the model function with τ_{imp} ~ 70 ms (blue). The proportionality constants derived in this way are used as a relative measure of the N impurity penetration factor.

dataset (discussed in Section 6), it was found that equally good fits could be obtained for a range of $\tau_p$values spanning from 50 to 100 ms. Therefore, it was not possible to extract a reliable value for τ_p by fitting the nitrogen brightness time response – but neither was it necessary. For long time scales, both model and brightness signals approach a quasi-steady state, as expected from Eq. (3). Therefore, the same analysis used for L-modes can be applied to H-modes: compute the ratio of HFS to LFS scale factors to deduce the HFS to LFS ratio of penetration factors, or more generally, contamination efficiencies. The only requirement was that a quasi-stationary nitrogen brightness signal must be observed. This restricted the analysis to only those plasmas that attained a long steady H-mode phase.

One additional concern was the possibility that the H-mode impurity confinement time, τ_p, might vary from shot-to-shot. Since the analysis relies on comparing identical shots – one with a HFS puff and one with a LFS puff – lacking information on τ_p would introduce uncertainty in the deduced penetration factor ratios. To inform this question, we performed Ca^{18+} confinement time measurements regularly during the study, sometimes late in the same plasma that was used

to perform the screening measurements. Reassuringly, we found that τ_p did not vary significantly. To further limit variability, we ran back-to-back identical discharges, alternately puffing from HFS and LFS locations, and repeating the sequence to verify reproducibility. Finally, for all the EDA H-modes analyzed we fixed the value of τ_p used in the model function, $M(t)$, to 70 ms. In effect, this ascribed differences in HFS/LFS scale factors to differences in penetration factor alone. As discussed above, this is merely a conceptual simplification since the scale factor ratio may, in any case, be interpreted as a measure of the relative contamination efficiency.

As seen in Fig. 4, we found that the N^{6+} brightness signals yielded better signal-to-noise ratios than the N^{5+} brightness data. Therefore, we report scale factors deduced from the ratio of N^{6+} brightness to either gas puff injection rate (for the case of negligible τ_p in L-modes and I-modes) or model function $M(t)$ with τ_p = 70 ms (for EDA H-modes). For L-mode discharges, we normalize them so that the relative penetration factor is unity for the case of a LFS nitrogen injection into a 0.8 MA balanced double-null plasma with Greenwald fraction of 0.2. For EDA H-mode and I-mode data, we normalize the relative penetration factors to be ~unity for a LFS puff into a balanced double-null.

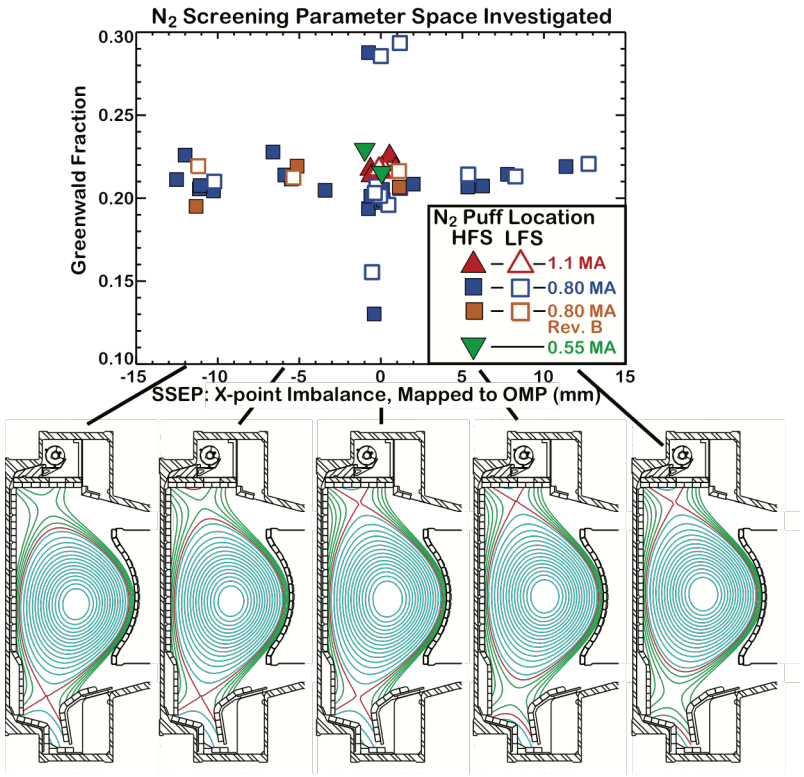

Fig. 5 – The SOL screening characteristics of 51 L-mode discharges were investigated with the values of Greenwald fraction, plasma current and magnetic topology shown. Upper/lower x-point imbalance is parameterized by the difference in major radius at the outer midplane of their poloidal flux surface mappings.

5. Impurity screening results: L-mode

5.1 Plasma conditions

Calibrated nitrogen injections were performed on 51 L-mode plasmas: 45 with $B \times \nabla B$ towards to lower x-point and 6 with $B \times \nabla B$ pointing away. All discharges had a toroidal field of 5.4 tesla. A variation in magnetic x-point balance was performed at fixed current and density (see Fig. 5). For magnetic topology near balanced double-null, a factor of two variation in plasma current (0.55, 0.8, 1.1 MA) was performed at fixed Greenwald fraction (i.e., line-averaged density normalized to the Greenwald density [29]) and factor of two variation in Greenwald fraction was performed (0.13 to 0.29) at fixed current. For the 6 cases with $B \times \nabla B$ pointing away from the lower x-point, a magnetic x-point balance scan was performed, spanning from double-null to lower single null. To facilitate a direct comparison of HFS versus LFS screening characteristics, identical plasmas were repeated in many cases, with the only change being the location of the nitrogen injection.

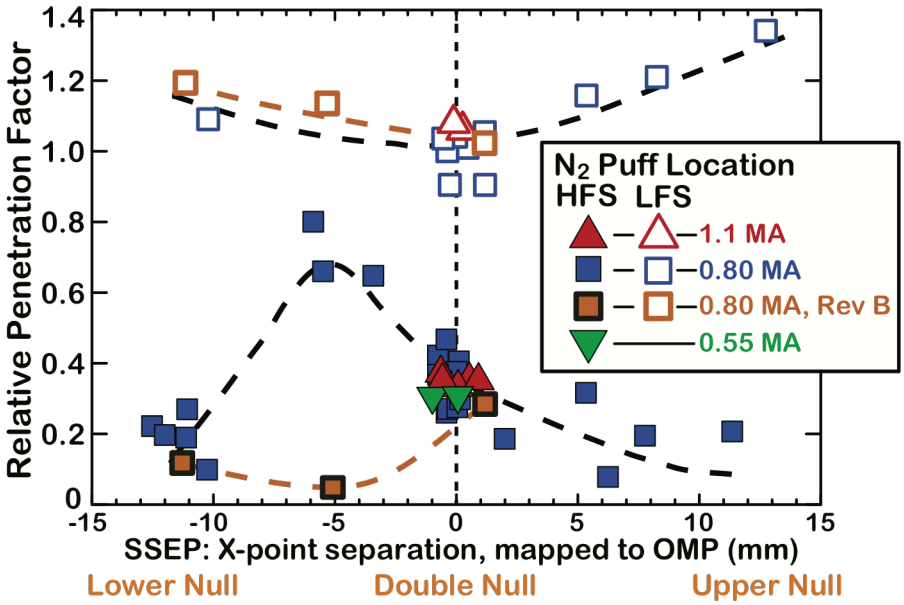

Fig. 6 – Relative nitrogen penetration factor as a function of upper/lower x-point separation (SSEP). Black dashed lines are added to guide the eye for forward field cases ($B \times \nabla B$ pointing toward lower x-point). Orange dashed lines track trends from reversed field cases ($B \times \nabla B$ pointed away from lower x-point) – these are not fits to the data. All data points shown in Fig. 5 are included in this plot. New data with reversed field (orange symbols) verify the hypothesis that $E \times B$ flows affect HFS impurity penetration factors; HFS impurity penetration drops by an order of magnitude at SSEP = - 5 mm when magnetic field direction is reversed.

5.2 HFS/LFS nitrogen penetration factors

Nitrogen penetration factors are shown in Fig. 6 for the L-mode data set. The forward field dataset was reported previously in [13]. Recently, we performed experiments with reversed magnetic field (orange symbols, $B \times \nabla B$ pointing away from lower x-point). The horizontal axis is a measure of upper/lower magnetic flux surface balance; it corresponds to the distance between flux surfaces that contain x-points, mapped to the outer mid-plane (SSEP). The penetration factors are normalized to the value obtained for a LFS injection into a 0.8 MA balanced double-null plasma with Greenwald fraction of 0.2. The nitrogen impurity penetration factors on the HFS SOL are found to be persistently lower than the LFS SOL, even for the cases of balanced double null, where the HFS profiles are extremely narrow (see Fig. 2). In this case, the HFS impurity penetration is a factor of 2.5 lower than LFS and remains at that value for a factor of 2 variation in plasma current at fixed Greenwald fraction and a factor of two variation in Greenwald fraction at fixed plasma current. (Note that the same set of data points shown in Fig. 5 is plotted in Fig. 6). As SSEP is increased to large positive or large negative values, HFS nitrogen impurity penetration becomes a factor of ~10 lower than LFS. This is consistent with earlier observations for single null cases [9].

While it is expected that impurity penetration might increase as magnetic topology attains balanced double null, it is perhaps unexpected that the highest impurity penetration factors occur for *unbalanced* double-null plasmas, with SSEP values around -5 mm for forward field cases. Because we were able to measure the SOL profiles on the HFS SOL (Fig. 2), we are confident that the SSEP values reported by magnetic flux measurements [30] and EFIT magnetic reconstruction [31] are accurate. When SSEP is reported to be zero, the HFS scanning probe reports a sharp fall-off in the SOL, roughly coincident with the location of the LCFS (see right panels in Fig. 2). When SSEP is small but non-zero, a 'shoulder' appears in the HFS SOL, consistent with the formation of common zone of poloidal flux that maps between HFS and LFS (see left panels in Fig. 2).

As discussed in [13], the leading explanation for the peak in nitrogen penetration factor for SSEP ~ -5 mm comes from recognizing that plasma flow in the SOL includes both parallel and perpendicular ($E \times B$) components; the overall rate that impurities are flushed to the divertor depends on whether these flows work together or in opposition. On open field lines, electron temperature profiles and plasma potential profiles are tightly coupled via the constraints of sheath physics and parallel thermal gradient forces in the electron fluid. As a result, the radial electric field in the SOL tends to point in the direction of minor radius. When $B \times \nabla B$ points away from the dominant divertor, both $E \times B$ and parallel flows in the HFS can be directed toward that divertor. When $B \times \nabla B$ points toward the dominant divertor, it is possible that the poloidal projections of $E \times B$ and parallel flows oppose, in which case the impurity flushing action can become reduced or stagnant.

As a direct test of this hypothesis, experiments were repeated with reversed toroidal magnetic field (5.4 tesla) and reversed plasma current (0.8 MA), keeping all other parameters the same. Figure 6 shows the additional penetration factor measurements, plotted as closed orange symbols for the HFS injection case and open symbols for LFS. The HFS impurity penetration factor for SSEP = -5 mm is seen to drop by an order of magnitude compared to forward field cases. On the other hand, HFS impurity penetration factors with reversed field are otherwise similar to forward field balanced double null cases and lower single null cases. LFS impurity penetration factors are

also similar. (Impurity penetration factors for reversed field are normalized so that PF is ~1 for the LFS balanced double null case.) These data present strong evidence that the peak in impurity penetration factor detected at SSEP = -5 mm for forward field L-modes was due to $E \times B$ drifts working in opposition to the parallel flow towards the lower divertor.

The forward and reversed field data also show that divertor geometry (and associated recycling of nitrogen from divertor surfaces) played, at best, a minor role compared to SOL transport physics in determining core nitrogen levels. Note that the target plate geometries of the upper and lower divertors on C-Mod are different: the upper has an open, horizontal plate configuration while the lower has a closed, vertical target plate configuration (see Fig. 1). If nitrogen recycling from these surfaces was impacting core contamination in any significant way, then the result from field reversal seen in Fig. 6 would not be so dramatic. It should also be noted that previous studies in C-Mod found that the divertor geometry (upper versus lower) had no influence on the SOL flows in the main chamber [7, 8]. For example, mid-plane HFS and LFS SOL flows for forward-B, lower single-null topology are the same as for reversed-B, upper single-null – as if the tokamak were simply turned upside down.

Further information on the SOL impurity transport physics was obtained by looking at HFS nitrogen impurity 'plume' dispersal patterns and their dependence on SSEP values. Key diagnostics for this study were visible cameras and a poloidally-resolved Lyman-alpha photodiode array. In order to compile a complete report on the impurity screening experiments, and to provide context for the EDA H-mode and I-mode results (Section 6), we first review measurements and observations made from forward-field ohmic L-mode discharges [13].

5.3 Nitrogen plume dispersal observations

5.3.1 "Maypole plume"

On selected plasmas, images of unfiltered visible light emission from the center column region in C-Mod were captured by two systems: a 'front view' camera in which the HFS N_2 gas injection location was visible and a 'back view' camera located 180 degrees toroidally from the former (see Fig. 7). In general, the typical response to a local impurity gas injection is the formation of a 'plume' of impurity ions, extending along and across magnetic field lines [20, 32]. The shape of the plume can provide information on background plasma flows in both the parallel and perpendicular ($E \times B$) directions. In preparation for the impurity screening experiments, some lower single-null plasmas where run with a large N_2 gas puff applied to the HFS mid-plane capillary. This produced a 'maypole plume' – a name given to a field-aligned emission pattern on the visible light cameras that wrapped around the center column down to the lower divertor.

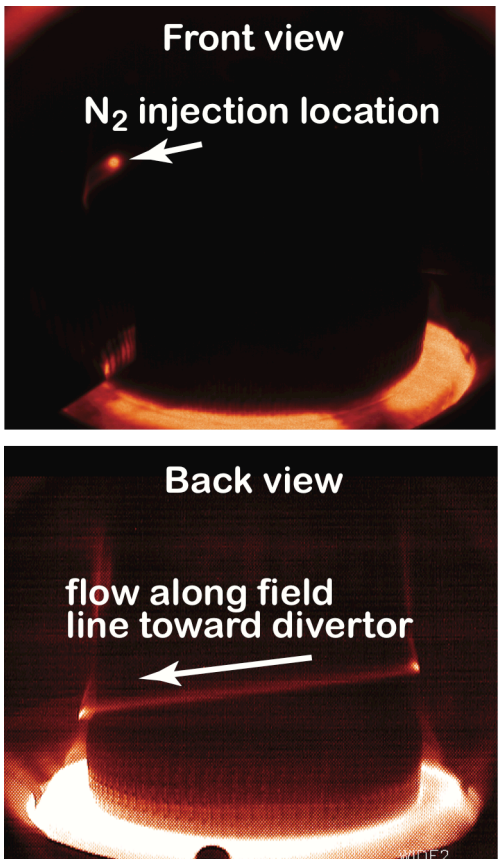

Fig. 7 – A 'maypole plume,' observed in unfiltered visible light emission (false color image is shown) for a lower single-null plasma with strong nitrogen puff from an inner-wall mid-plane capillary tube, directly illustrates strong parallel flows to the divertor and the 'quiescent' nature of the HFS SOL. Reprinted from [13] http://dx.doi.org/10.1016/j.nme.2016.10.006 https://creativecommons.org/licenses/by-nc-nd/4.0/Copyright

This observation clearly illustrates the 'quiescent' nature of the HFS SOL. The plume is seen to extend uninterrupted for a very long distance (~ 4 meters) compared to the SOL width (few mm). The unidirectional nature of the plume and its long parallel extent is consistent with measurements of near-sonic parallel flows in the HFS SOL [25] directed toward the lower divertor for this magnetic topology. These images also illustrate directly how a SOL may efficiently screen wall-born impurities: if the conditions are right, the impurities may be swept away preferentially to the divertor rather than enter the confined plasma. The HFS SOL is unique in this regard. No such streamers have been observed when nitrogen was puffed at the LFS mid-plane.

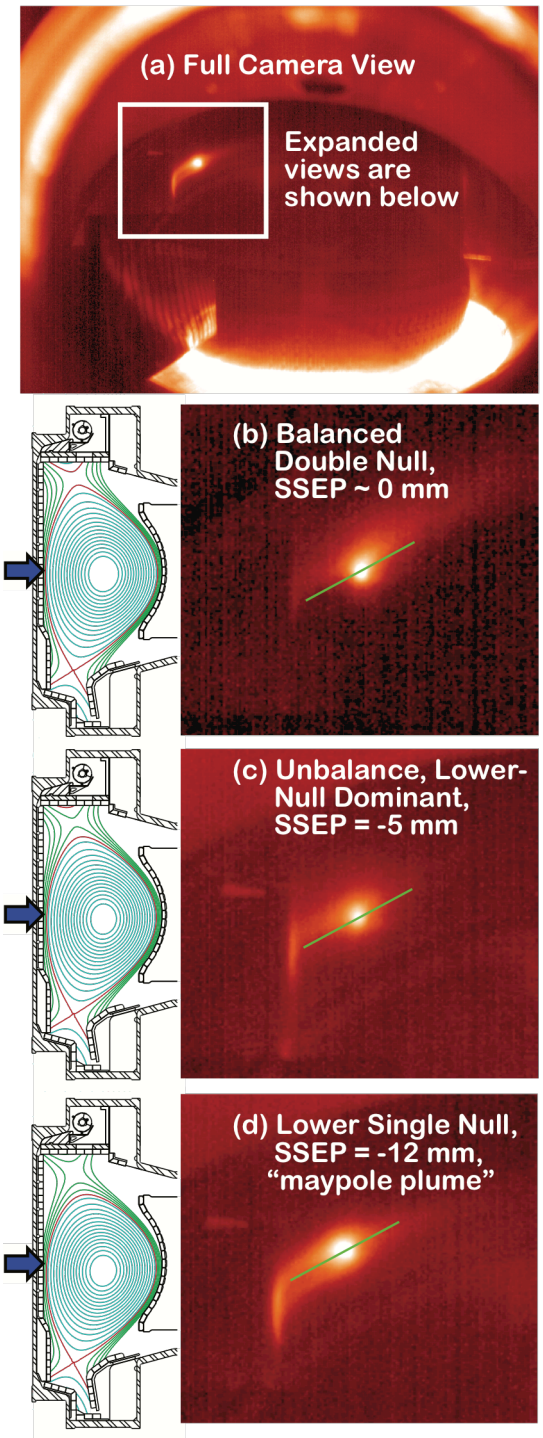

Fig. 8 – Camera images of nitrogen injection plume: (a) upper single null, (b) balanced double-null, (c) unbalanced, lower null dominant, and (d) lower single null magnetic configurations. Reprinted from [13] http://dx.doi.org/10.1016/j.nme.2016.10.006 https://creativecommons.org/licenses/by-nc-nd/4.0/Copyright

5.3.2 Plume dispersal images

In an effort to understand why the HFS impurity penetration is maximized for an unbalanced double null configuration with SSEP ~ -5 mm (forward-field, ohmic L-mode plasmas), plume dispersal images captured by the 'front camera' view of Fig. 7 were examined for different SSEP values. Figure 8 shows cases of (b) *balanced double null*, (c) *unbalanced double null* (SSEP ~ -5 mm), and (d) *lower single null* (SSEP ~ -12 mm). The corresponding magnetic equilibria are also shown. The magnetic equilibrium for case (d), *lower single null*, is identical to that for the 'maypole plume' shown in Fig. 7 but the nitrogen flow rate was reduced by about a factor of two, consistent with levels used for cases (b) and (c). To guide the eye, a green line is drawn on panel (d), aligned with the plume streamer. A green line with the same orientation is shown on panels (b) and (c).

The plume dispersion pattern in panel (b), *balanced double null,* does not indicate a preferential flow direction along field lines. Instead, this plume exhibits a classic 'boomerang' pattern [32], which is indicative of a strong $E \times B$ drift (in this case directed towards the upper divertor) that competes with spreading along magnetic field lines in both directions. The plume dispersal pattern in panel (c), *unbalanced, lower-null dominant*, shows evidence of a directed flow, but the streamer is not field-aligned. The pattern suggests an ($E \times B$) drift toward the upper divertor combined with a flow along the magnetic field line toward the lower divertor.

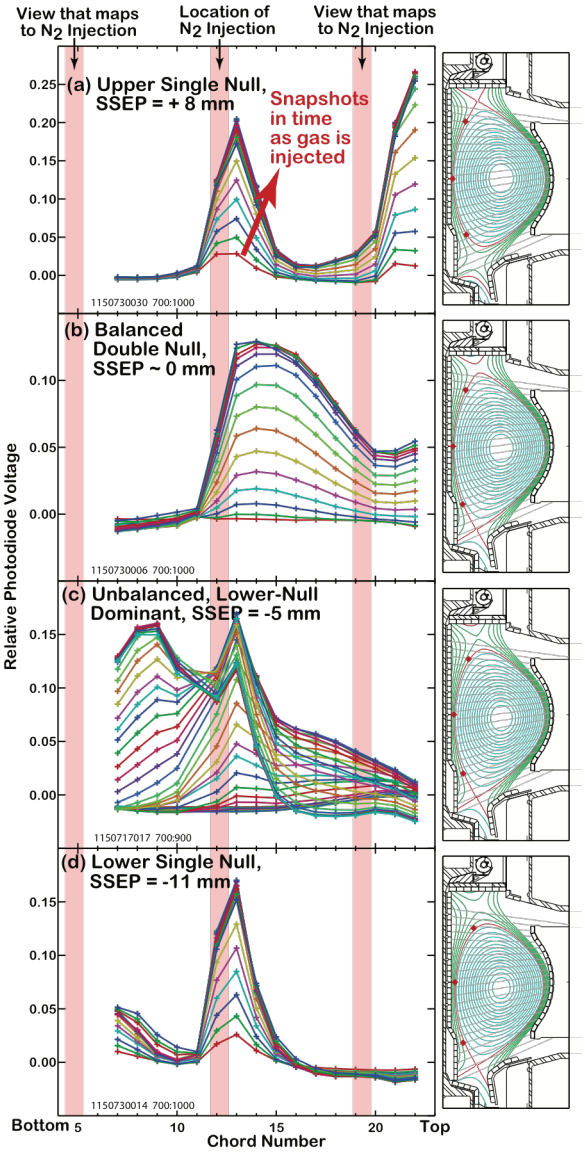

Fig. 9 – Ly_α photodiode array measurements of HFS nitrogen injection plumes. Red symbols on equilibrium plots (right panels) indicate where a magnetic field line that starts at the gas puff location passes in front of the diode array as it wraps around the torus. These locations are also indicated as vertical red bands on the photodiode data (left panels). Overlaid profile 'snapshots' show the time evolution, starting from when the gas puff is turned on to when the peak flow rate is approached. Data from chords 1-6 are unreliable and therefore not shown. Reprinted from [13] http://dx.doi.org/10.1016/j.nme.2016.10.006 https://creativecommons.org/licenses/by-nc-nd/4.0/Copyright

Overall, these dispersal patterns are consistent with idea that both parallel and $E \times B$ flows contribute to the net rate in which wall-born impurities are swept to the active divertor. Moreover, for the case when impurity penetration is observed to be maximized, SSEP ~ -5 mm, it appears that the nitrogen impurities may, in effect, circle around the center column with little or no directed motion towards either divertor.

5.3.3 Photodiode array observations

A UV-enhanced photodiode array, constructed to record Ly_α emission in the boundary plasma [33], was found to provide high quality information about nitrogen impurity plume dispersal. This system consisted of an array of bandpass filtered photodiodes viewing UV emission in the Ly_α wavelength range (120 nm center, 8.6 nm FWHM) along horizontal chords at different elevations (see Fig. 9). Fortuitously, this spectral band can also be used to monitor the concentration of N^{4+} ions, taking advantage of bright 2p-2s lines at 123.88 and 124.28 nm [34]. The use of N^{4+} emission characterizes the plume from the near SOL while the visible emission discussed above is from lower ionization stages closer to the capillary injector. Both techniques allow the full SOL to be characterized.

The toroidal location of the diode array was coincident with the location of the HFS gas puff capillary tube. As a result, chords 12 and 13 directly viewed the injection point. For situations in which the N^{4+} ion dispersal is extended along field lines over long distances (for example, the "maypole plume"), the array can detect the streamer again as it circles around the center column. Information from the diode

array can therefore help determine if the plume emission pattern was field-aligned and/or exhibited a strong $E \times B$ drift. The red symbols on the magnetic flux surfaces plots in Fig. 9 mark the trajectory of magnetic field lines at three points: at the gas injection location and again were the field lines cross in front of the diode array after one transit around the torus. Vertical bands on the photodiode profiles indicate where a field-aligned emission pattern would appear in the profile. Photodiode voltage data are shown for four magnetic configurations: (a) *upper single null*, (b) *balanced double-null*, (c) *unbalanced, lower null dominant*, and (d) *lower single null*. The multiple profiles shown for each case track the evolution in time of photodiode signals, starting from the beginning of the gas puff to when a steady nitrogen flow was established. Baseline signal levels are subtracted, with the baseline corresponding to a 100 ms time average taken before the puff. For all cases, a strong signal is seen on mid-plane chords near point of N_2 injection. But in general, the emission is not centered about the point of injection. The central emission peak tends to shift to higher elevations, depending on the specific magnetic equilibrium. As discussed in [13], the photodiode profiles and their sensitivity to magnetic equilibrium reveal important details about impurity dispersal in the HFS SOL:

a) *upper single null* – In this case the mid-plane peak is narrow and a second peak appears at the highest elevation. The location of the second peak does not correspond to a strict field line mapping (red vertical band) but appears above it. There is essentially no emission below the inner mid-plane. The emission pattern is consistent with a field-aligned plume heading to the upper divertor, but perhaps with the assist of an upwards $E \times B$ drift.
b) *balanced double-null* – In this case the mid-plane peak is strongly skewed toward the upper chamber. There is no emission below the inner mid-plane. This emission pattern is consistent with the 'boomerang' plume seen in Fig. 8b; it is indicative of a very strong $E \times B$ drift of the nitrogen impurities toward the upper divertor.
c) *unbalanced, lower null dominant* – A mid-plane peak is observed but the emission pattern is very broad, favoring an asymmetry towards the upper divertor early in time and an asymmetry towards the lower divertor late in time. The pattern late in time shows a second peak below the mid-plane. The location of this peak does not correspond to a strict field line mapping (red vertical band) but appears significantly above it. Early in time, this emission pattern hints at a strong upward drift, and later in time a field-aligned plume heading to the lower divertor, but with a strong upwards $E \times B$ contribution.
d) *lower single null* – In this case the mid-plane peak is narrow again and there is a hint of another peak occurring at the lowest elevation. The emission pattern is consistent with a field-aligned plume heading to the lower divertor, but perhaps with some upwards $E \times B$ contribution as well.

These impurity plume dispersal observations provide clear evidence that both parallel and $E \times B$ flows affect the impurity dispersion and rate in which impurities are swept out of the local SOL. The observations are consistent with HFS penetration factors being largest for the *unbalanced, lower null dominant* case (SSEP = -5 mm) with normal magnetic field direction. The new reversed field data (orange symbols in Fig. 6) directly support this hypothesis. In this situation, $E \times B$ and parallel flows should point in the same direction, sending impurities toward the lower divertor. As a result, HFS impurity penetration should be very low, as is observed.

6. Experimental results: EDA H-mode and I-mode

6.1 EDA H-mode

EDA H-modes [35, 36] are stationary, high confinement plasmas in which edge pedestal gradients are relaxed via a continuous 'quasi-coherent mode' (QCM) [19, 37] rather than by intermittent ELM-like events. EDA discharges do not accumulate impurities, making them ideal candidates for impurity screening investigations. A series of good quality EDA H-modes (21 total) was produced with toroidal field of 5.4 tesla, plasma currents of 0.55 MA and attaining typical Greenwald fractions of 0.35. ICRF heating (second harmonic H minority in D majority plasma) was applied at the level of 1.4 MW, resulting in a total input power of approximately 1.7

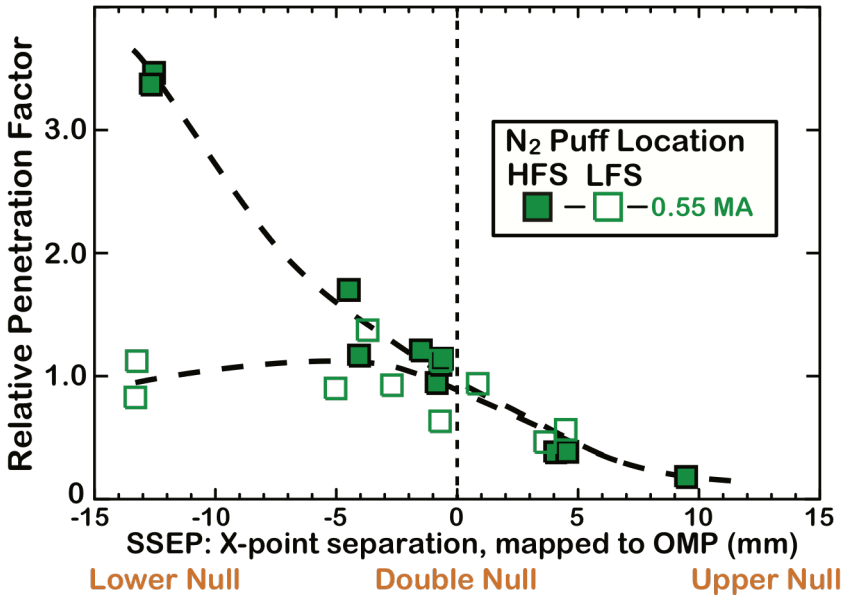

Fig. 10 – Relative nitrogen penetration factor for 0.55 MA, 5.4 tesla EDA H-mode plasmas as a function of upper/lower x-point separation (SSEP). B × ∇B is pointing toward the lower x-point. Dashed lines are added to guide the eye – these are not fits to the data.

MW. All plasmas were similar, exhibiting characteristic density and temperature pedestals and a QCM. Magnetic topology was scanned from lower single-null to double null to upper-single null with forward magnetic field direction (B × ∇B pointing toward the lower x-point). ITER $H_{98,y2}$ confinement factors [38] were typically 0.9, with the exception of discharges with the smallest values of SSEP (~ -12 mm, lower single-null), which had $H_{98,y2} \sim 0.7$. This may be due in part to the reduced elongation and reduced upper triangularity (see plasma shapes in Fig. 11). Relative nitrogen penetration factors were recorded for HFS and LFS gas puffs (Fig. 10), using the technique outlined in section 3.

Figure 10 shows some interesting and unanticipated trends. Unlike the L-mode discharges (Fig. 6), no clear difference is observed in HFS/LFS impurity penetration factors, with the exception of lower-single null cases where the HFS penetration factor *exceeds LFS by a factor of 3*. In addition, the LFS penetration factor exhibits a dependence on magnetic topology, becoming reduced as the magnetic flux balance favors upper null. Unfortunately, we were not able to

obtain any more LFS screening data point to explore this trend for SSEP ~ +10 mm. In order to verify that the large values of HFS impurity penetration for SSEP ~ -12 mm were not spurious, we performed repeated measurements, producing the four data points shown. These were very well matched discharges in which the only change was the application of HFS versus LFS puffs. It should be noted that 'high recycling' plasma conditions were obtained at the inner divertor target plate in these lower single-null plasmas, with electron temperatures around 10 eV and densities in the range of 1-2 x 10^{20} m^{-3}. There was no evidence of a MARFE-like event in the divertor or x-point regions.

Despite the somewhat puzzling dependence of HFS penetration factor on SSEP and the sharp increase for SSEP ~ -12 mm, the overall result is favorable to the idea of implementing HFS RF launchers and operating in near double-null configurations. HFS impurity penetration is no

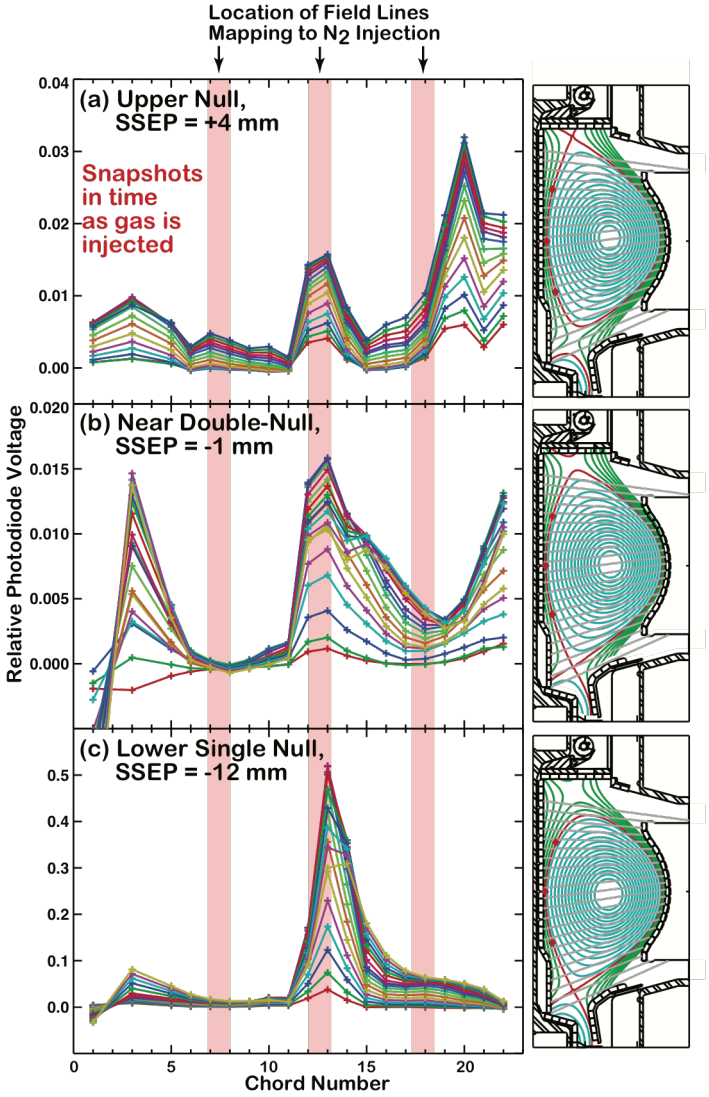

Fig. 11 – Ly_α photodiode array measurements of HFS nitrogen injection plume in EDA H-mode for (a) upper single null, (b) balanced double-null, and (d) lower single null magnetic configurations.

worse than LFS. There may be some advantage in operating at slightly positive values of SSEP.

The photodiode array 17 (Fig. 11) provide some clues as to why the HFS impurity screening becomes poor for the lower-single null case, again involving the influence of $E \times B$ drifts. The format of the plots shown Fig. 11 is similar to that of Fig. 9, but with data from chords 1, 2, 3, 5 and 6 now included. However, it is important to note that chords 1-6 view plasma recycling from the inner divertor target.

a) *Upper-null* – The plume emission pattern in this case has features that are similar to the L-mode discharge (Fig. 9a). The mid-plane peak is narrow and a second peak occurs at the highest elevation, which is shifted above the location where a strict field line mapping would place it (red vertical band). The emission pattern is consistent with a field-aligned plume heading to the upper divertor, but with the assist of an upwards $E \times B$ drift. (Diode signals from the lower divertor target also rise with the puff, but these may be contaminated by residual nitrogen recycling light and or changes in Ly_α emission due to recycling from that region.)
b) *Near double-null* – The plume emission pattern in this case also has features that are similar to the corresponding L-mode discharge (Fig. 9b) – the mid-plane peak is strongly skewed toward the upper chamber, suggestive of a 'boomerang' plume with strong $E \times B$ drift of the nitrogen impurities toward the upper divertor.
c) *Lower single null* – This plume emission pattern hints as to why the HFS impurity penetration is so efficient in this configuration for EDA H-modes. Despite the fact that this is a lower-single null discharge, this emission pattern remains highly skewed toward the upper divertor. There is no evidence that parallel flows are able to carry impurities into the lower divertor at all; the photodiode signals at the mid-plane greatly exceed signals from the lower divertor channels. We therefore conclude that the SOL $E \times B$ flows in EDA H-mode are so strong as to overwhelm parallel impurity flows into the divertor, even for a lower single-null discharge. Apparently, due to the competing flows, the impurities are not able leave the SOL and reach either the upper or lower divertor surfaces. This is similar to the *unbalanced, lower null dominant* case for L-modes (Fig. 9 c) but now extended to much more negative SSEP values.

These observations highlight the complexity of impurity dispersal in the SOL, involving interactions with both parallel and $E \times B$ flows – and these flows depend not only on magnetic topology and magnetic field direction but also on local conditions in the SOL, which in turn may be influenced by the plasma confinement mode.

In retrospect, it may have been instructive to repeat the above EDA H-mode experiments with a plasma current of 0.8 MA, similar to the L-mode data set. In this situation, the increased pitch angle of the magnetic field in the HFS SOL might allow parallel flows to compete more effectively against opposing $E \times B$ flows, sweeping impurities to the lower divertor in the lower single null case.

6.2 I-mode

I-modes [39, 40] are stationary, high confinement plasmas that do not exhibit ELMs. In this case, edge pedestal gradients are relaxed via a continuous, 'weakly-coherent mode' (WCM), coupled to edge geodesic acoustic modes (GAMs). I-modes exhibit an edge thermal transport barrier but lack a particle transport barrier. Consequently, these discharges do not form a density pedestal and have impurity confinement times that are similar to L-modes [24]. I-modes are attained with the help of operating in the 'unfavorable' $B \times \nabla B$ drift direction, i.e., with $B \times \nabla B$ pointing away from the active x-point. In this situation, the H-mode power threshold is increased. Consequently, high input power levels can be applied to the I-mode, particularly at high toroidal magnetic fields. For these screening studies, 9 good quality I-mode plasmas were produced with a toroidal field of 5.4 tesla, plasma current of 0.8 MA and attaining typical Greenwald fractions of 0.14. ICRF heating was applied at the level of 2.2 MW, resulting in a total input power of approximately 2.7 MW. All I-modes were similar, exhibiting the characteristic temperature pedestal but lacking a density pedestal and attained typical $H_{98,y2}$ confinements factors of 0.9. Magnetic topology was scanned from lower single-null to near double null with *reversed* magnetic field direction. Relative nitrogen penetration factors were recorded for HFS and LFS gas puffs (Fig. 12), using the technique outlined in section 3.

Although the penetration factors exhibit more scatter than L-modes and EDA H-modes, HFS impurity penetration factors are seen to be consistently lower than LFS in I-mode, by roughly a factor of two. This is perhaps not unexpected. $E \times B$ and parallel flows work in the same direction to remove impurities to the active divertor in the magnetic configuration that favors I-mode ($B \times \nabla B$ pointing away from the active x-point). These results are favorable to the idea of employing HFS RF launchers with I-mode confinements regimes.

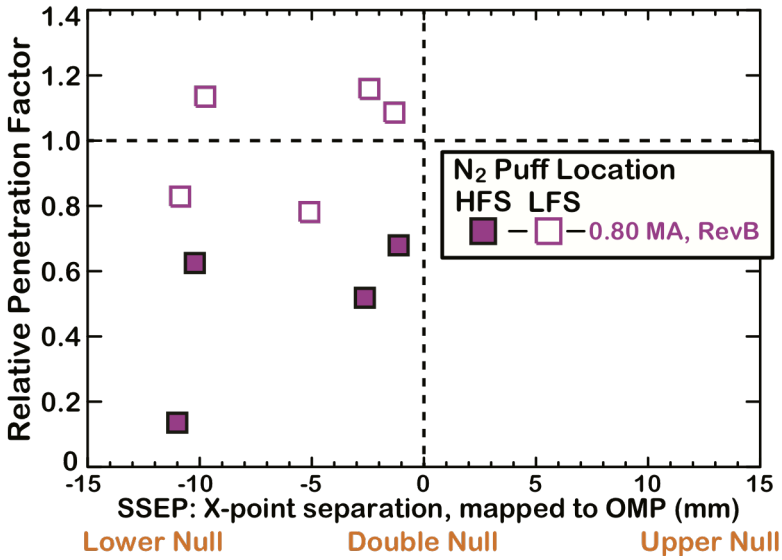

Fig. 12 – Relative nitrogen penetration factor as a function of upper/lower x-point separation (SSEP) for 9 I-mode plasmas in which the magnetic field direction was reversed ($B \times \nabla B$ pointing away from the lower x-point).

Photodiode observations (Fig. 13) tell a familiar and expected story for these lower x-point favored geometries with *reversed* magnetic field:

a) *Near double-null* – The plume emission pattern is similar to that from EDA H-mode in a near double-null configuration (Fig. 11b), i.e., a mid-plane peak that is strongly skewed, except that it is skewed toward the lower chamber – clear evidence of an $E \times B$ drift effect. Emission in the lower divertor is very strong; parallel flows may also be contributing to the impurity removal. There is essentially zero emission in the upper divertor.

b) *Lower single null* – $E \times B$ sm earing of the mid-plane emission peak is weak, yet the lower divertor emission is strong, with the emission starting at the point at which a field-aligned plasma flow would carry impurities into the divertor (left vertical red band). There is essentially zero emission in the upper divertor.

Taken together, the HFS/LFS impurity screening results from the L-, H- and I-mode plasmas tell a consistent story. Despite the fact that the HFS SOL has very narrow profiles in balanced double-null configurations, impurities injected at the HFS mid-plane do not experience a higher penetration factor compared to the LFS mid-plane. In many cases, the screening of impurities is more effective. Parallel and $E \times B$ flows play a role and, through the external 'control knob' of magnetic flux balance, these flows can be made to help or hinder the screening characteristics of wall-born impurities in the HFS SOL.

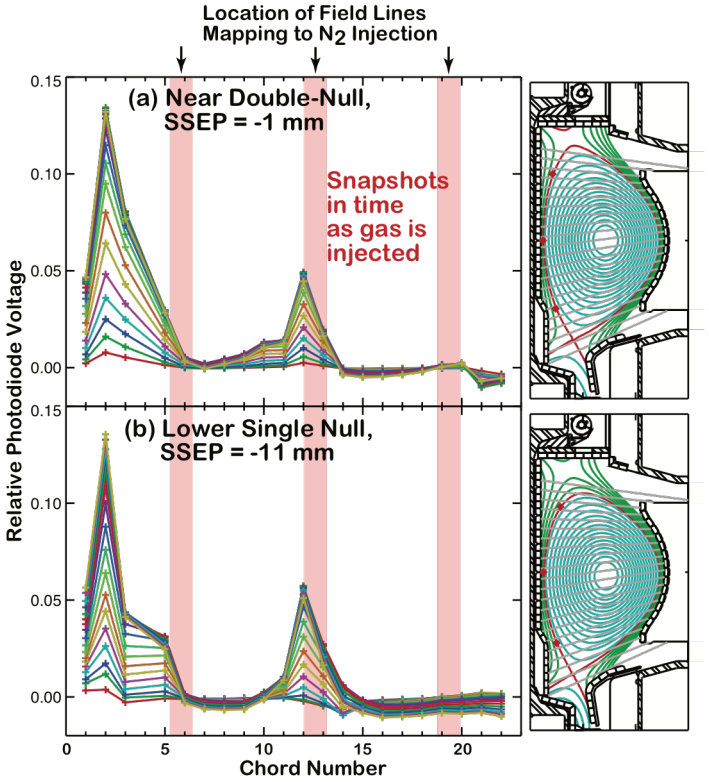

Fig. 13 – Ly_α photodiode array measurements of HFS nitrogen injection plume in I-mode for (a) near balanced double-null, and (b) lower single null magnetic configurations with reversed magnetic field ($B \times \nabla B$ pointing away from the lower x-point).

7. Summary and conclusions

Impurity screening responses of the high-field and low-field side scrape-off layers to local nitrogen injection have been compared in Alcator C-Mod for different magnetic equilibria (upper single-null, balanced double-null, lower single-null) and different core plasma confinement modes. Building on previous results from L-modes [13], new data are reported for reversed field L-modes, EDA H-modes and I-modes.

The research is motivated by the need to demonstrate mitigation and control of plasma-material interactions on main-chamber components to acceptable levels for fusion power plants. A promising idea is to take advantage of the low turbulence, quiescent nature of the HFS SOL: place all PMI-sensitive, close fitting first-wall components, including RF actuators, on the high-field side of the tokamak and operate in near-double null magnetic configurations. The concept of placing RF launchers on the high-field side is compelling for many reasons, including: favorable wave physics on the HFS that projects to significant increases in current drive efficiency and effectiveness; precise control of local plasma conditions at the antenna/plasma interface via magnetic configuration control, allowing PMI to be minimized and wave coupling to be optimized – even dynamically; the HFS is a zone of natural protection against runaway electrons, ELMs and energetic particles. Previous experiments in Alcator C-Mod found that the screening of nitrogen impurity ions by the HFS SOL is a factor of ~10 better than that of the LFS SOL in single-null magnetic topologies [9]; the lack of turbulence on the HFS [7], combined with very strong 'transport driven' parallel flows to the divertor [8], were believed to be responsible. However, in double-null configurations, the HFS SOL becomes very narrow and parallel flows are not as strong. The research described in this paper therefore sought to answer key questions: Does the favorable HFS screening behavior extend to balanced double-null configurations? Or, is operation with a balanced double null configuration a clear *disadvantage* with regard to core plasma impurity control?

Nitrogen contamination levels in the core plasma were monitored and compared as nitrogen gas was injected on the HFS and LFS mid-planes in otherwise identical plasmas. The screening behavior of the local scrape-off layer was quantified in terms of an *impurity penetration factor*. The behavior of nitrogen – a non-intrinsic low-recycling species in C-Mod – has taken as a proxy for the behavior of local wall-born impurity sources. Based on an investigation of 51 L-mode discharge (6 with reversed magnetic field), 21 EDA H-modes, and 9 I-mode discharges, a consistent picture of the impurity screening behavior of the HFS scrape-off layer and the physical mechanisms that control it emerged:

1. Despite the formation of an extremely thin scrape-off layer on the HFS with very sharp n_e, T_e profiles in balanced double-null, the HFS SOL is found to screen locally injected nitrogen just as effectively as the LFS SOL – sometimes a factor of 2 or more better – depending on specific conditions. This result is favorable to the idea of locating RF actuators on the HFS.
2. The impurity screening effectiveness of the HFS SOL is determined by both parallel and perpendicular ($E \times B$) flows.
3. Based on impurity plume dispersion observations, $E \times B$ flows carry impurities in the

direction opposite to $B \times \nabla B$ in the HFS SOL; this corresponds to a radial electric field pointing in the minor radius direction in the SOL.

4. In situations in which the $E \times B$ drift opposes and effectively competes against (i.e., cancels) the poloidal projection of parallel flow to the active divertor, HFS SOL screening tends to be least effective. This was encountered in two situations: L-modes with a slight magnetic imbalance favoring the lower x-point with $B \times \nabla B$ pointing toward the lower x-point and low current (0.55 MA) EDA H-modes operating with a lower single-null geometry ($B \times \nabla B$ pointing toward the lower x-point). In the former case, HFS screening was reduced but still remained a factor of 1.5 more effective than LFS screening. But in the latter case, HFS screening became *a factor of 3 less effective* than LFS screening, despite being similar in a balanced double null configuration. Based on the present physics understanding, one might expect that HFS impurity screening in this situation would depend on plasma current; changing the pitch of the magnetic field lines on the HFS could affect the competition between parallel and $E \times B$ flows. However, no data on this are available at this time.
5. In situations in which $E \times B$ and parallel flows work together to sweep impurities to the active divertor, HFS SOL screening tends to be very effective. This result was shown clearly in comparing data from forward and reversed field L-modes with magnetic flux imbalance slightly favoring the lower x-point (Fig. 6). In the best of circumstances, HFS screening can be a factor of 10 more effective than LFS while at the same time attaining a near double-null magnetic configuration. I-modes seem to take advantage of this effect. HFS screening was typically a factor of 2 more effective than LFS over the range of magnetic geometries available to I-mode. Since I-modes are attained with $B \times \nabla B$ drift in the 'unfavorable' direction, they always have $E \times B$ and parallel flows working together to remove impurities from the HFS SOL.

In conclusion, these experiments showed that the impurity screening behavior of the HFS SOL is very favorable to the idea of employing near double-null plasmas for PMI control for first-wall components, including RF actuators. Dynamic control of magnetic flux balance and HFS wall-plasma gap has the potential to be an extremely powerful tool – controlling the scrape-off layer conditions and PMI at antenna-plasma interfaces; controlling the plasma flows that sweep away wall-born impurities into the divertor. Future tokamaks should be designed to take advantage of this behavior.

Acknowledgements
Alcator C-Mod's unique contributions to the advancement of fusion energy science over the past 24 years have been made possible by an excellent team of very dedicated engineers, technicians, students, and scientists. This work was supported by DoE Contract DE-FC02-99ER54512 on Alcator C-Mod, a DoE Office of Science user facility.

References

[1] Abdou, M., et al., Fusion Engineering and Design 100 (2015) 2.
[2] Podpaly, Y.A., Olynyk, G.M., Garrett, M.L., Bonoli, P.T., and Whyte, D.G., Fusion Engineering and Design 87 (2012) 215.
[3] Sorbom, B.N., et al., Fusion Engineering and Design 100 (2015) 378.
[4] LaBombard, B., et al., Nucl. Fusion 55 (2015) 053020.
[5] Wallace, G.M., et al., Submittted to Fusion Engineering and Design (2017)
[6] Kessel, C.E., et al., Submitted to Fusion Engineering and Design (2017)
[7] Smick, N., LaBombard, B., and Hutchinson, I.H., Nucl. Fusion 53 (2013) 023001.
[8] LaBombard, B., et al., Nucl. Fusion 44 (2004) 1047.
[9] McCracken, G.M., et al., Phys. Plasmas 4 (1997) 1681.
[10] Wallace, G.M., et al., "Development of lower hybrid current drive actuators for reactor relevant conditions," presented at the 41st EPS Conference on Plasma Physics and Controlled Fusion, Berlin, Germany, 2014.
[11] Bonoli, P.T., et al., "Novel Reactor Relevant RF Actuator Schemes for the Lower Hybrid and the Ion Cyclotron Range of Frequencies," Preprint: 2016 IAEA Fusion Energy Conference, Kyoto [TH/5-1].
[12] Bonoli, P.T., et al., Bull. Am. Phys. Soc. 59 (2014) 363.
[13] LaBombard, B., et al., Nuclear Materials and Energy (2017)
http://www.sciencedirect.com/science/article/pii/S2352179116300400.
[14] Hutchinson, I.H., et al., Phys. Plasmas 1 (1994) 1511.
[15] Marmar, E.S., Fusion Science and Technology 51 (2007) 261.
[16] Greenwald, M., et al., Phys. Plasmas 21 (2014) 110501.
[17] Smick, N. and LaBombard, B., Rev. Sci. Instrum. 80 (2009) 023502.
[18] LaBombard, B. and Lyons, L., Rev. Sci. Instrum. 78 (2007) 073501.
[19] LaBombard, B., et al., Phys. Plasmas 21 (2014) 056108.
[20] Jablonski, D., et al., J. Nucl. Mater. 241-243 (1997) 782.
[21] Reinke, M.L., et al., Rev. Sci. Instrum. 81 (2010) 10D736.
[22] Howard, N.T., Greenwald, M., and Rice, J.E., Rev. Sci. Instrum. 82 (2011) 033512.
[23] Ince-Cushman, A., et al., Rev. Sci. Instrum. 79 (2008) 10E302.
[24] Rice, J.E., et al., Nucl. Fusion 55 (2015) 033014.
[25] Smick, N., LaBombard, B., and Pitcher, C.S., J. Nucl. Mater. 337-339 (2005) 281.
[26] Boswell, C.J., Terry, J.L., LaBombard, B., Lipschultz, B., and Pitcher, C.S., Plasma Phys. Control. Fusion 46 (2004) 1247.
[27] Thompson, M.W., Philosophical Magazine 18 (1968) 377.
[28] Stangeby, P.C., The plasma boundary of magnetic fusion devices Peter C. Stangeby (Institute of Physics Pub., Bristol, UK ; Philadelphia, PA, 2000).
[29] Greenwald, M., Plasma Phys. Control. Fusion 44 (2002) 27.
[30] Granetz, R.S., Hutchinson, I.H., Gerolamo, J., Pina, W., and Tsui, C., Rev. Sci. Instrum. 61 (1990) 2967.
[31] Lao, L.L., St. John, H., Stambaugh, R.D., Kellman, A.G., and Pfeiffer, W., Nucl. Fusion 25 (1985) 1611.
[32] Gangadhara, S. and LaBombard, B., Plasma Phys. Control. Fusion 46 (2004) 1617.
[33] Faust, I.C., et al., Phys. Plasmas 23 (2016) 056115.
[34] Loarte, A., et al., Phys. Plasmas 18 (2011) 056105.
[35] Greenwald, M., et al., Phys. Plasmas 6 (1999) 1943.
[36] Hubbard, A.E., et al., Phys. Plasmas 8 (2001) 2033.
[37] Snipes, J.A., et al., Plasma Phys. Control. Fusion 43 (2001) L23.

[38] ITER Physics Basis Expert Groups on Confinement and Transport and Confinement Modelling and Database, ITER Physics Basis Editors 1999 Nucl. Fusion 39 2175.
[39] Whyte, D.G., et al., Nucl. Fusion 50 (2010) 105005.
[40] Hubbard, A.E., et al., Nucl. Fusion 56 (2016) 086003.